Effect of bending stiffness on the deformation of liquid capsules enclosed by thin shells in shear flow

Duc Vinh Le*
*A*STAR Institute of High Performance Computing, 1 Fusionopolis Way, No. 16-16 Connexis, Singapore 138632, Singapore*
(Received 8 April 2010; published 29 July 2010)

Shear-induced deformation of liquid capsule enclosed by thin shell causes the development of in-plane tensions and bending moments due to the shell thickness or to a preferred three-dimensional unstressed configuration. This paper considers the effect of bending stiffness due to a preferred three-dimensional structure on the deformation and motion of the liquid capsule. To perform the numerical simulations, an improved formulation for computing the forces generated on the capsule surface during deformation is proposed. This formulation takes full account of large deformation kinematics and the development of in-plane tensions and bending moments. The deformation and orientation dynamics of capsules with different reference shapes are studied under various shear rates, viscosity ratios, and bending modulus. The numerical results show that the bending stiffness not only restricts the deformation but also affects the motion mode of the capsules. In addition, raising bending stiffness amplifies the shape deformation oscillations in tank-treading mode but reduces the oscillations in tumbling mode.

DOI: 10.1103/PhysRevE.82.016318 PACS number(s): 47.55.−t, 46.70.−p

I. INTRODUCTION

The mechanical properties of plasma membranes have been shown in recent years to play an important role in physiology and cell biology. An archetypal system for study is the erythrocyte membrane of which the elastic properties determine many of the flow characteristics of blood and enable the red blood cells (RBCs) to deform and migrate in the blood vessels. The interest in the mechanical properties of the erythrocyte membrane stems from multiple sources. For example, blood disorder such as sickle cell anemia has been shown to be associated with structural alterations in the erythrocyte membrane and the resulting changes in mechanical response [1]. In addition, useful mechanical properties of the RBC membrane suggest potential synthetic applications such as synthetic capsules with polymerized membranes in drug delivery.

Much effort has been devoted to study the dynamics of red blood cells and synthetic capsules in the flows using experimental [2–6], analytical [7–10], and numerical [11–17] methods. Experimental and theoretical studies have revealed complex interaction of different physical properties of the capsule and the fluid that affect the deformations of the suspended capsule in the flow. In a simple shear flow, capsules exhibit primarily two types of motion [18–20]: a tank-treading motion in which the capsule shape and orientation are steady and the membrane rotates continuously as a tank tread, and a tumbling motion in which the capsule undergoes a periodic flipping motion. Recently, swinging motion in which the capsule exhibits periodic oscillations in both deformation and orientation superimposed on a tank-treading mode has been observed both experimentally [6,21] and computationally [22–24].

The type of motion a capsule or RBC undergoes depends on capsule shape, viscosity ratio between the internal and suspending fluids, applied shear rate, and membrane flexural stiffness. The membrane stiffness is determined by the modulus of elasticity for in-plane deformation and bending modulus. Bending stiffness is believed to play an important part in determining the equilibrium configuration and the deformation of biological membranes consisting of lipid bilayers, including the membrane of red blood cells [13,25]. However, little effort has been devoted to investigate the effect of bending stiffness on the deformation and motion of the capsule and most of the previous theory and numerically studies neglected bending resistance. Pozrikidis [13] proposed a formalism that allowed the coupling of bending moments and membrane tensions to the fluid mechanics and thereby facilitated numerical simulations for the capsule deformation. The effect of bending stiffness on the shear-induced deformation of liquid capsules in Stokes flow has also been illustrated in [13]. However, significant inaccuracies and numerical instabilities arise at high deformation due to inadequate spatial resolution and very small time step is required for stability in the presence of bending moments. Another restriction is the requirement that the reference shape has a uniform curvature. Sui *et al.* [15] studied the effect of bending stiffness on the deformation of two-dimensional (2D) elastic capsules in shear flow. Although the 2D study maintains most common features of the three-dimensional (3D) capsule motion, it does not capture the effect of bending stiffness on the deformation of the full 3D capsule in quantitative terms.

In the present study, we model the capsule membrane as a thin shell that develops the bending moments by two physical mechanisms. First, stresses developing over the cross section of the thin shell may be integrated over the shell thickness to yield the tangential bending moments. These tangential bending moments have neglected effect on the deformation of very thin membrane. However, these bending moments play a crucial role in the determination of the folding pattern of the membrane including wrinkles and their number and size [26]. Second, bending moments are generated due to a preferred three-dimensional unstressed configu-

*ledv@ihpc.a-star.edu.sg

ration of the membranes consisting of lipid bilayers [25]. The corresponding energy function of the membrane may be expressed in terms of membrane curvatures and bending modulus [27]. This bending modulus accounts for the bending flexural stiffness and is generally distinct from the elastic modulus for in-plane deformation. Owing to the extreme thinness of the membrane, we only consider the effect of bending moments generated due to a preferred three-dimensional unstressed configuration.

In the present work, the numerical method is based on the implicit immersed boundary method [24,28] with subdivision thin-shell model [29] for simulating large deformation of liquid capsules immersed in the fluid. The implicit method allows using relative large time step without loss of stability especially in the presence of bending resistance. The numerical stability can be improved further by the use of the subdivision surface [30] to represent the capsule membrane.

Our goals in this work are as follows. First is to extend our previous work on thin-shell model [24,29] to take into account the bending moments generated due to the preferred three-dimensional unstressed configuration of the membrane. Consideration of the effect of these bending moments is motivated by a need to develop an integrated model to study fluid-structure interaction. In this model, the equations of shell mechanics are developed in surface curvilinear coordinates and implemented in terms of the principle of virtual displacements. Second is to investigate the effect of bending stiffness on the deformations as well as the types of motion of capsules with various unstressed shapes in shear flow. Simulations are performed for different dimensionless shear rates and viscosity ratios under a broad range of bending flexural stiffness.

II. FORMULATION AND NUMERICAL METHOD

In the present study, we consider the shear-induced deformation of a capsule containing a viscous fluid and suspended in another fluid of different viscosity. During the capsule deformation, the capsule membrane develops anisotropic tensions and bending moments. In describing the kinematics of the capsule membrane, we adopt the thin-shell model [31,32] formulated based on the Kirchhoff-Love hypothesis.

A. Kinematic description of the shell

Consider a shell body Ω_S whose undeformed thickness is denoted by $\bar{h}$ and undeformed and deformed middle surfaces are denoted by $\bar{\Gamma}$ and Γ, respectively. The surface basis vectors corresponding to $\bar{\Gamma}$ and Γ are

$$\bar{\boldsymbol{a}}_\alpha = \bar{\boldsymbol{X}}(\xi^1,\xi^2)_{,\alpha}, \quad \boldsymbol{a}_\alpha = \boldsymbol{X}(\xi^1,\xi^2)_{,\alpha}, \tag{1}$$

respectively, where $\bar{\boldsymbol{X}}$ and $\boldsymbol{X}$ are the positions of a material point associated with the curvilinear coordinates (ξ^1,ξ^2) on the shell middle surface in its undeformed and deformed configurations, respectively. Here and henceforth, a comma is used to denote partial differentiation, greek indices take the values of 1 and 2 and lowercase latin indices range from 1 to 3. The local covariant basis vectors on the undeformed and deformed configurations are defined as

$$\bar{\boldsymbol{g}}_\alpha = \bar{\boldsymbol{a}}_\alpha + \xi^3 \bar{\boldsymbol{a}}_{3,\alpha}, \quad \bar{\boldsymbol{g}}_3 = \bar{\boldsymbol{a}}_3,$$

$$\boldsymbol{g}_\alpha = \boldsymbol{a}_\alpha + \xi^3(\eta \boldsymbol{a}_3)_{,\alpha}, \quad \boldsymbol{g}_3 = \eta \boldsymbol{a}_3, \tag{2}$$

where ξ^3 is the thickness coordinate, η is the thickness stretch, and $\bar{\boldsymbol{a}}_3$ and $\boldsymbol{a}_3$ are the unit normal vectors to the middle surfaces. Contravariant basis vectors $\bar{\boldsymbol{g}}^i$ and $\boldsymbol{g}^i$ are defined such that $\bar{\boldsymbol{g}}_i \cdot \bar{\boldsymbol{g}}^j = \delta_i^j$ and $\boldsymbol{g}_i \cdot \boldsymbol{g}^j = \delta_i^j$, where δ_i^j is the Kronecker delta. The corresponding covariant and contravariant components of the metric tensors in both configurations are

$$\bar{g}_{ij} = \bar{\boldsymbol{g}}_i \cdot \bar{\boldsymbol{g}}_j, \quad g_{ij} = \boldsymbol{g}_i \cdot \boldsymbol{g}_j,$$

$$\bar{g}^{ij} = \bar{\boldsymbol{g}}^i \cdot \bar{\boldsymbol{g}}^j, \quad g^{ij} = \boldsymbol{g}^i \cdot \boldsymbol{g}^j. \tag{3}$$

In terms of the covariant and contravariant basis vectors, the deformation gradient tensor $\mathbf{F}$ for the shell body may be expressed in the form

$$\mathbf{F} = \frac{\partial \boldsymbol{X}}{\partial \bar{\boldsymbol{X}}} = \frac{\partial \boldsymbol{X}}{\partial \xi^i} \otimes \bar{\boldsymbol{g}}^i = \boldsymbol{g}_i \otimes \bar{\boldsymbol{g}}^i, \tag{4}$$

where here and henceforth summation over the repeated index i is implied in the range from 1 to 3.

B. Equilibrium deformations of hyperelastic shells

To describe the mechanical response of the thin shell we assign strain-energy functions W, per unit undeformed volume of $\bar{\Omega}$, and H, per unit area of Γ, respectively. The total strain energy of the thin shell is defined by

$$S = \int_{\bar{\Omega}_S} W d\bar{\Omega}_S + \int_\Gamma H d\Gamma. \tag{5}$$

For the incompressible hyperelastic material, we consider the neo-Hookean elastic energy function per unit undeformed volume,

$$W = \frac{E}{6}(g_{ij}\bar{g}^{ij} - 3), \tag{6}$$

where E is the Young's modulus. To model for the RBC membrane, we use the strain-energy function proposed by Skalak *et al.* [33] and given in [24]. In addition, we consider the Helfrich [27] bending energy function for biological membranes, given by

$$H = 2\kappa_B(\kappa_m - \kappa_m^R)^2, \tag{7}$$

where κ_B is the scalar bending modulus and κ_m^R is the reference mean curvature. The mean curvature κ_m is computed as $\kappa_m = \kappa_{\alpha\beta} g^{\alpha\beta}/2$, where $\kappa_{\alpha\beta} = \boldsymbol{a}_{\alpha,\beta} \cdot \boldsymbol{a}_3$ is the component of the curvature tensor.

The Kirchhoff stress tensor can be expressed as

$$\boldsymbol{\tau} = \tau^{ij} \boldsymbol{g}_i \otimes \boldsymbol{g}_j, \tag{8}$$

with the components $\tau^{ij} = 2(\partial W/\partial g_{ij}) - p_s g^{ij}$, where p_s denotes the hydrostatic pressure. The hydrostatic pressure can be calculated from the plane stress assumption by requiring that $\tau^{33} = 0$. The thickness strain g_{33} and thickness stretch η can be computed from the incompressibility condition,

det $\mathbf{F}=1$. Following [31,32], we define the stress resultant $\boldsymbol{n}^i$ and the moment resultant $\boldsymbol{m}^\alpha$ as

$$\boldsymbol{n}^i = \int_{-\bar{h}/2}^{\bar{h}/2} \boldsymbol{\tau}\cdot\boldsymbol{g}^i \bar{\nu} d\xi^3,$$

$$\boldsymbol{m}^\alpha = \int_{-\bar{h}/2}^{\bar{h}/2} \boldsymbol{\tau}\cdot\boldsymbol{g}^\alpha \xi^3 \bar{\nu} d\xi^3, \tag{9}$$

where $\bar{\nu}$ accounts for the curvature of the shell in the volume integration. The bending stress follows from Eq. (7) by the work conjugacy, with the result

$$q^{\alpha\beta} = \frac{\partial H}{\partial \kappa_{\alpha\beta}} = 2\kappa_B(\kappa_m - \kappa_m^R)g^{\alpha\beta}. \tag{10}$$

To derive the equilibrium equations of the shell body in weak form, we start from the fact that the potential energy of the shell body is stationary at equilibrium, i.e.,

$$\delta\Pi = \delta\Pi_{\text{int}} + \delta\Pi_{\text{ext}} = 0, \tag{11}$$

where $\delta\Pi_{\text{ext}}$ is the variation of the potential energy of the external forces. The variation of the potential of the internal forces can be expressed as

$$\delta\Pi_{\text{int}} = \int_{\bar{\Omega}_S} \frac{\partial W}{\partial \mathbf{F}} : \delta\mathbf{F} d\bar{\Omega}_S + \int_\Gamma \frac{\partial H}{\partial \kappa_{\alpha\beta}} \delta\kappa_{\alpha\beta} d\Gamma. \tag{12}$$

Substituting Eq. (4) into Eq. (12) and through a straightforward manipulation we arrive at the following formulation:

$$\int_{\bar{\Gamma}} [\boldsymbol{n}^\alpha \cdot \delta\boldsymbol{a}_\alpha + \eta\boldsymbol{n}^3 \cdot \delta\boldsymbol{a}_3 + \boldsymbol{m}^\alpha \cdot (\eta\delta\boldsymbol{a}_3)_{,\alpha}] d\bar{\Gamma}$$
$$+ \int_\Gamma q^{\alpha\beta}[\delta\boldsymbol{a}_{\alpha,\beta}\cdot\boldsymbol{a}_3 + \boldsymbol{a}_{\alpha,\beta}\cdot\delta\boldsymbol{a}_3] d\Gamma + \delta\Pi_{\text{ext}} = 0. \tag{13}$$

Details for the derivation of the first integral of Eq. (12) were given in [24,31].

C. Spatial discretization of the thin shell

Here, we follow the C^1-interpolation scheme based on the subdivision surface proposed in [29,31] for thin-shell analysis. The main idea behind subdivision surfaces is to represent the smooth shell middle surface by a control mesh containing a set of NP control points $\mathbf{x}_I$, where $I=1,\ldots,\text{NP}$. This mesh may be taken as a basis for introducing an interpolation of the form

$$\mathbf{x}(\xi^1,\xi^2) = \sum_I N^I(\xi^1,\xi^2)\mathbf{x}_I, \tag{14}$$

where I is the local numbering of the nodes and $N^I(\xi^1,\xi^2)$ is the box-spline basis function [30]. Introducing the interpolated parametric Eq. (14) into the weak form (13), we arrive at the formulation for the internal force at node I as

$$\boldsymbol{f}_I = \int_{\bar{\Gamma}} \left[\boldsymbol{n}^\alpha \cdot \frac{\partial \boldsymbol{a}_\alpha}{\partial \mathbf{x}_I} + \eta\boldsymbol{n}^3 \cdot \frac{\partial \boldsymbol{a}_3}{\partial \mathbf{x}_I} + \boldsymbol{m}^\alpha \cdot \left(\eta \frac{\partial \boldsymbol{a}_3}{\partial \mathbf{x}_I}\right)_{,\alpha}\right] d\bar{\Gamma}$$
$$+ \int_\Gamma q^{\alpha\beta}\left[\left(\frac{\partial \boldsymbol{a}_\alpha}{\partial \mathbf{x}_I}\right)_{,\beta}\cdot\boldsymbol{a}_3 + \boldsymbol{a}_{\alpha,\beta}\cdot\frac{\partial \boldsymbol{a}_3}{\partial \mathbf{x}_I}\right] d\Gamma. \tag{15}$$

The internal force at node I is the sum of element contributions as in the standard finite element method. The contribution to the internal force at node I from a generic element can be calculated by a one-point quadrature rule [31] with the barycenter of the element as the Gaussian quadrature point. The stress and moment resultants at the quadrature point are computed by numerical integration of the stresses across the thickness of the shell using the three-point Simpson rule.

D. Front-tracking method

The coupling between the fluid and the capsule deformation is done using a front-tracking method that is based on the implicit immersed boundary method [28]. In this method, the force density is computed at the control points and is distributed to a fixed (Eulerian) fluid grid using a discrete representation of the delta function,

$$\boldsymbol{f}(\boldsymbol{x},t) = \sum_{I=1}^{\text{NP}} \boldsymbol{f}_I(\xi^1,\xi^2,t) D_h(\boldsymbol{x}-\mathbf{x}_I(t))\Delta\xi^1\Delta\xi^2, \tag{16}$$

where $\boldsymbol{f}_I(\xi^1,\xi^2,t)$ is the force per unit area at the control point $\mathbf{x}_I$ whose label is (ξ^1,ξ^2). Here, $\boldsymbol{x}$ is the Eulerian grid and $D_h(\boldsymbol{x})$ is a three-dimensional discrete delta function [34]. Once the force density is computed at the control points and distributed to the grid, the Navier-Stokes equations with the forcing terms are then solved for the pressure and velocity field $\boldsymbol{u}(\boldsymbol{x},t)$ [28]. The velocity field is then interpolated to find the velocity at the control points, which is used to advance the position of the thin shell, $\mathbf{x}_I$, in time in an implicit manner [24,28].

In the numerical simulations, we consider capsules with spherical and oblate spherical initial shapes and biconcave capsules resembling the resting shapes of red blood cells. To describe an oblate spheroid with aspect ratio of b/a, we use the mapping $x_{obl}=Rx$, $y_{obl}=Ry$, $z_{obl}=(b/a)Rz$, where (x,y,z) is the coordinate of a point on the unit sphere and the radius R is adjusted to preserve the volume. Similarly, to describe the biconcave disk shape assumed by red blood cells at rest, we use the mapping [35]

$$x_{rbc} = Rx, \quad y_{rbc} = Ry,$$

$$z_{rbc} = \pm 0.5R\sqrt{1-r^2}(C_0 + C_1 r^2 + C_2 r^4),$$

where $r^2=x^2+y^2\le 1$, $C_0=0.2072$, $C_1=2.0026$, and $C_2=-1.1228$.

To test the development of bending moments, we study the relaxation of capsules in the fluid under the influence of bending moments alone. The reference configuration of the shell is a flat sheet with zero mean curvature and the viscosity ratio is unity. Figure 1(a) shows the evolution of the trace of the surface of an ellipsoidal capsule with axes ratio 2:2:1 in the (x,z) plane at a sequence of dimensionless time

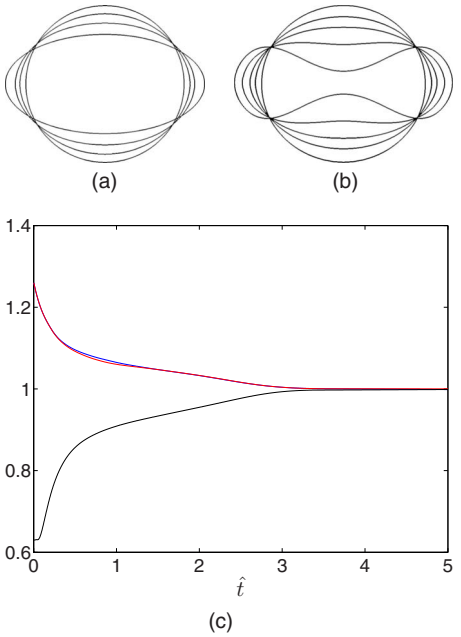

FIG. 1. (Color online) Relaxation of (a) an ellipsoid with axes ratio 2:2:1 at $\hat{t}=0,0.25,0.75,5.0$ and (b) a biconcave disk at $\hat{t}=0,0.2,0.5,1.4,5.0$. (c) Convergence of the three axes of the spheroid shown in (a), normalized to a_{eq}.

$\hat{t}=t\kappa_B/(\mu a_{eq}^3)$. Here, a_{eq} is the radius of the sphere that has the same volume as that of the considering capsule and μ is the suspending fluid viscosity. Figure 1(b) shows the corresponding evolution of a biconcave disk. In both cases, the capsules relax gradually to steady states with spherical shapes. Figure 1(c) illustrates the convergence of the three axes of the ellipsoidal capsule to the steady state. The simulations presented in Fig. 1 were performed with dimensionless time step $\Delta\hat{t}=\Delta t\kappa_B/(\mu a_{eq}^3)=0.005$, which is about ten times larger than that used in [13]. The capsules converge to the stationary spherical shapes without numerical instabilities. The change in the volume of the capsules was less than 0.03%, which is typical of all simulations presented in the next section.

III. RESULTS

The present method is used to study the deformation of capsules enclosed by thin shells with spherical, spheroidal, and biconcave unstressed shapes in simple shear flow given by the velocity $\boldsymbol{u}=(\dot{\gamma}z,0,0)$, where $\dot{\gamma}$ is the shear rate. Simulations are performed for different dimensionless shear rates $G=\mu\dot{\gamma}a_{eq}/(E\bar{h})$, reduced bending modulus $\hat{\kappa}_B=\kappa_B/(a_{eq}^2E\bar{h})$, and viscosity ratios λ. The equivalent volumetric radius a_{eq} is chosen to be sufficiently small so that the inertia effect is neglected. The center of the capsule is placed at the center of a cube of side $10a_{eq}$. This computational domain is large enough so that boundary effects are not important [36,37]. Boundary conditions for the velocity are of the Dirichlet type at $z=\pm 5a_{eq}$ and periodic at other boundaries. In the subsequent simulations, the initial capsule shape is taken to be a reference state for the in-plane tensions. Simulations are performed on a $96\times96\times96$ fluid grid with an unstructured surface mesh of 10 242 nodes and 20 480 elements. The deformation of the capsule is described by the Taylor shape parameter $D_{xz}=(L-B)/(L+B)$, where L and B are the maximum and minimum radial distances of an ellipsoid with the same inertia tensor [12].

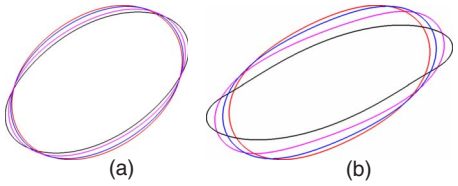

FIG. 2. (Color online) Contours of deformed stationary capsules with spherical initial shape at (a) $G=0.05$, $\hat{\kappa}_B=0,0.01,0.025,0.0375$ and (b) $G=0.2$, $\hat{\kappa}_B=0,0.04,0.1,0.15$.

A. Spherical capsules

The effect of bending stiffness on the deformation of spherical capsules enclosed by neo-Hookean thin shells in the shear flow is studied by varying the reduced bending modulus $\hat{\kappa}_B$. The reference shape concerning the bending moments is a flat sheet with vanishing reference curvature. Simulations were performed for two dimensionless shear rates G at $\lambda=1$ and different bending moduli. The results show that the initial spherical capsules deform to nearly ellipsoidal steady shapes which are inclined with respect to the x axis at well-defined angles, and the capsule membranes rotate around the interior fluid in a tank-treading mode [12]. Figure 2(a) shows the contours of deformed stationary capsules in the (x,z) plane at $G=0.05$ and $\hat{\kappa}_B=0,0.01,0.025,0.0375$. Figure 2(b) shows the corresponding contours at higher shear rate $G=0.2$ and $\hat{\kappa}_B=0,0.04,0.1,0.15$. As expected, the bending stiffness restricts the overall capsule deformation. An increase in the bending modulus $\hat{\kappa}_B$ leads to smaller deformation and reduced alignment with the undisturbed flow. This can be seen from the evolution of the Taylor deformation parameter and inclination angle in Fig. 3. The same effect has been observed in [13,15]. The results are compared with those obtained using the boundary element method (BEM) [13] and Fig. 3 shows reasonable agreement between the two methods.

Additional simulations were performed for viscosity ratio $\lambda=5$. Figure 4 shows the evolution of the deformation parameter and inclination angle at $G=0.05$ and $\hat{\kappa}_B=0,0.01,0.025,0.0375$. The figure confirms the effect of bending stiffness on the capsule deformation and orientation. The deformation parameter and inclination angle are compared with those obtained in [13,24]. At $\hat{\kappa}_B=0$, Fig. 4 shows excellent agreement between the present algorithm with subdivision elements and the thin-shell model with quadratic triangular elements [24]. For nonzero bending modulus, good agreement between the present method and the BEM [13] can also be observed in Fig. 4.

B. Oblate spherical capsules

Here, we consider a neo-Hookean oblate spheroid of aspect ratio $b/a=0.9$, inclined at the angle $\theta_0=\pi/4$ with re-

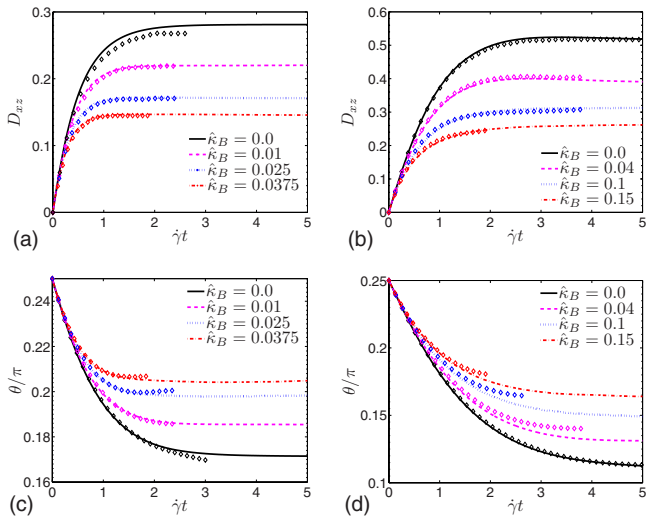

FIG. 3. (Color online) Evolution of deformation parameter D_{xz} for (a) $G=0.05$ and (b) $G=0.2$; inclination angle for (c) $G=0.05$ and (d) $G=0.2$. The diamonds are obtained using the BEM [13].

spect to the streamlines of the unperturbed flow. The initial oblate spherical shape is taken to be a reference state for the bending moments. The deformation parameter D_{xz} and the inclination angle θ are calculated for $G=0.05$, $\lambda=1$ at four different bending moduli $\hat{\kappa}_B=0.0,0.005,0.01,0.025$. As can be seen in Fig. 5, the oblate spheroid capsules undergo periodic oscillations in both the deformation parameter and the inclination angle superimposed on the tank-treading motion for all bending moduli. This mode of motion has also been observed in [6,23] and is referred to as swinging motion. At $\hat{\kappa}_B=0$, Sui *et al.* [15] observed a steady tank-treading mode in their 2D calculation which is different from the swinging mode observed in the present 3D calculation and in [12,24]. Since the oblate spheroid with $b/a=0.9$ is a nearly spherical capsule, its deformation trends are similar to those of the spherical capsule. An increase in the bending modulus $\hat{\kappa}_B$ at constant G and λ leads to smaller deformation and decreased alignment with the undisturbed flow. In the swinging mode, increasing bending modulus amplifies the oscillations in both the deformation parameter and the inclination angle. The numerical results also show that raising the bending modulus increases the oscillation frequency and tank-treading frequency. However, when the capsule exhibits tumbling mo-

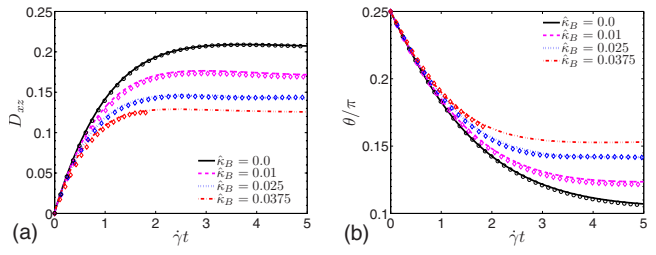

FIG. 4. (Color online) Evolution of the (a) deformation parameter and (b) inclination angle at $\lambda=5$ and $G=0.05$. The solid lines are obtained by the present algorithm with subdivision elements, and the circles are found using the quadratic triangular elements [24]. The diamonds are obtained using the BEM [13].

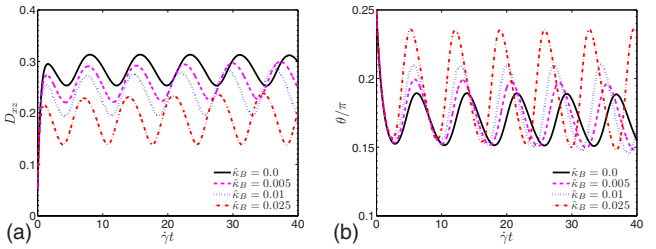

FIG. 5. (Color online) Evolution of (a) the deformation parameter and (b) inclination angle for oblate spheroidal capsules with $b/a=0.9$ at $G=0.05$ and $\lambda=1$.

tion in which the capsule undergoes continuous rotation as shown in Fig. 6(b), raising bending modulus reduces the oscillations in the deformation parameter. Figures 6(a) shows the evolution of the deformation parameter for the oblate capsules with $b/a=0.9$ at $G=0.005$ and $\hat{\kappa}_B=0.0,0.01,0.02,0.05$. Moreover, raising bending modulus reduces the oscillations in the phase angle [23] as seen in Fig. 6(c). We note that the phase angle δ is defined to quantify the oscillations in the swinging and tumbling modes as

$$\delta(t) = \alpha(t) - \theta(t) - [\alpha(0) - \theta(0)],$$

where $\alpha(t)$ is the tank-treading angle of a marker point on the membrane compared to the undisturbed flow direction. To make $\delta(t)$ a continuous function of time, we manually subtract π from $\alpha(t)$ or $\theta(t)$ after their values make a half rotation. If we increase $\hat{\kappa}_B$ further the oscillations in both the deformation parameter and phase angle will reduce toward the value of zero corresponding to a rotating solid ellipsoid.

In addition to restricting the deformation, bending stiffness can also affect the motion mode of the capsule. Figure 7(a) shows the time evolution of the inclination angle at $G=0.008$, $\lambda=1$ for three different bending moduli $\hat{\kappa}_B=0.0,0.002,0.005$. It can be seen that the capsule exhibits swinging motion at $\hat{\kappa}_B=0$ and tumbling motion at $\hat{\kappa}_B=0.005$. At $\hat{\kappa}_B=0.002$, we observe transient dynamics from

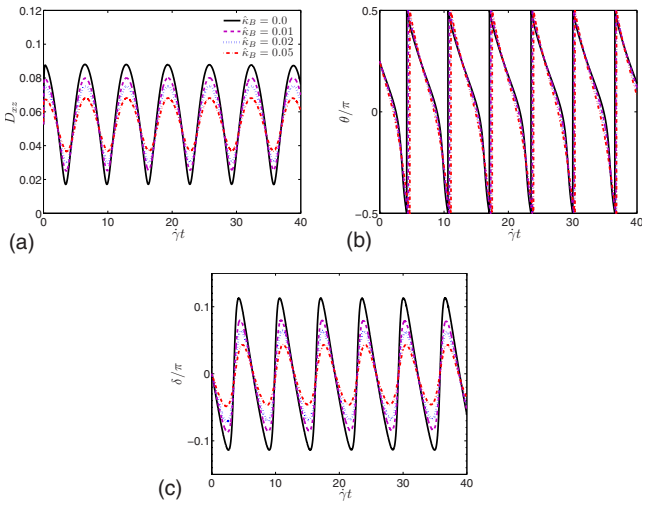

FIG. 6. (Color online) Evolution of (a) the deformation parameter, (b) inclination angle, and (c) phase angle for oblate spheroidal capsules with $b/a=0.9$ at $G=0.005$ and $\lambda=1$.

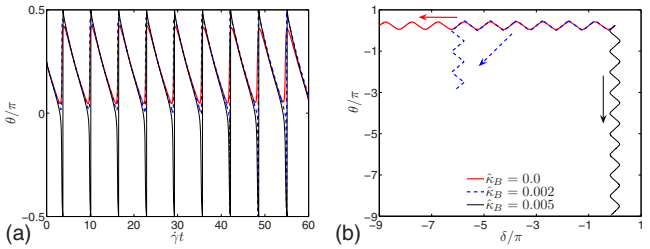

FIG. 7. (Color online) (a) Evolution of inclination angle and (b) typical plot of inclination angle θ vs phase angle δ for oblate spheroidal capsules with $b/a=0.9$ at $G=0.008$, $\lambda=1$.

swinging to tumbling. Figure 7(b) shows the corresponding plot of inclination angle θ vs phase angle δ for oblate spheroidal capsules at different states of motion. The arrows indicate the direction of time in the plot. In the swinging motion the inclination angle θ undergoes periodic oscillations while the phase angle δ changes monotonically with time. In the tumbling motion, the inclination angle θ changes monotonically with time while the phase angle δ undergoes periodic oscillations around a stationary value. Transition from swinging to tumbling is represented by the dashed line in Fig. 7(b).

Additional simulations were performed for the oblate capsule with viscosity ratio $\lambda=5$. Figure 8 shows the evolution of the deformation parameter and inclination angle at $G=0.05$ and $\hat{\kappa}_B=0,0.005,0.01,0.025$. Similar effect of bending stiffness on the capsule deformation and orientation was observed as in Fig. 5 for smaller viscosity ratios. We can notice that an increase in the viscosity ratio λ at constant G and $\hat{\kappa}_B$ leads to smaller deformation and greater alignment with the undisturbed flow.

C. Biconcave capsules

Next, we perform simulations for the biconcave capsules with Skalak's strain-energy function [24] for red blood cell membrane. In this energy function, the area dilatation modulus is chosen to be large enough to maintain the constant area of the biconcave capsule. The initial biconcave shape is also the reference shape concerning elastic tensions and bending moments. The healthy red blood cell membrane has the elastic modulus $E\bar{h}$ and bending modulus κ_B on the order of 10^{-3} dyn/cm and 10^{-12} dyn cm, respectively [25]. Taking the volume of a red blood cell to be $V\approx 7\times 10^{-11}$ cm^3, the

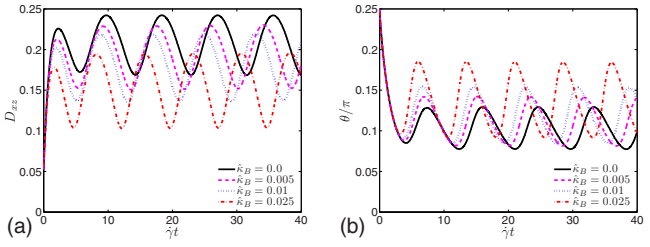

FIG. 8. (Color online) Evolution of (a) the deformation parameter and (b) inclination angle for oblate spheroidal capsules with $b/a=0.9$ at $G=0.05$, $\lambda=5$, and $\hat{\kappa}_B=0,0.005,0.01,0.025$.

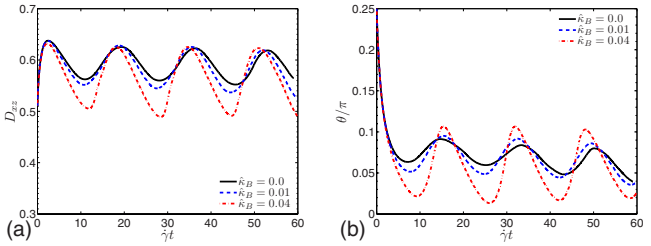

FIG. 9. (Color online) Evolution of (a) the deformation parameter and (b) inclination angle for biconcave capsules at $G=0.5$, $\lambda=2$, and $\hat{\kappa}_B=0,0.01,0.04$.

reduced bending modulus $\hat{\kappa}_B$ is then on the order of 10^{-2}. Hence, simulations are performed for bending moduli $\hat{\kappa}_B=0.0$, 0.01, and 0.04 at various dimensionless shear rates and viscosity ratios. Figure 9 shows the deformation parameter and inclination angle of a biconcave capsule with $\lambda=2$, initially inclined at 45° with respect to the x axis at $G=0.5$. Simulations suggested that the capsules deform to nearly stationary shapes while undergoing shape oscillations, with the membrane rotating around the inner fluid in a swinging mode. As expected, the bending stiffness restricted the deformation of the capsules. As the bending modulus increases, the oscillation amplitude of the deformation parameter and inclination angle becomes larger. This trend is similar to that of the oblate spheroid considered previously. Without bending stiffness, the dimple of the biconcave capsules disappears as observed in [29]. When there is bending modulus the capsules try to keep the instantaneous curvature as closed as

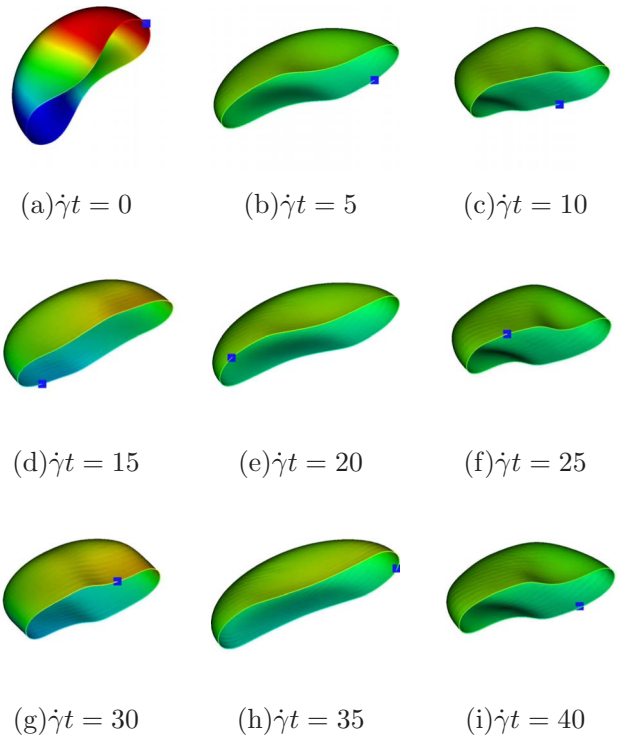

FIG. 10. (Color online) Shapes of the biconcave capsules at $G=0.5$, $\lambda=2$, and $\hat{\kappa}_B=0.04$ during a tank-treading motion. The colors represent the x component of the velocity on the surface of the capsule.

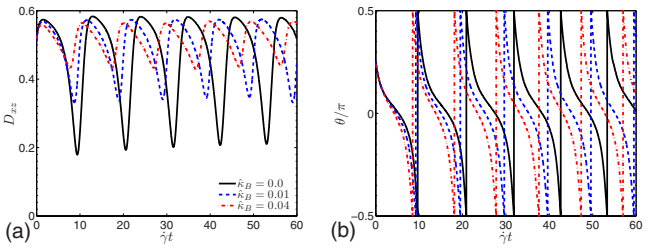

FIG. 11. (Color online) Evolution of the (a) deformation parameter and (b) inclination angle for biconcave capsules at $G=0.1$, $\lambda=4$, and $\hat{\kappa}_B=0, 0.01, 0.04$.

possible to the spontaneous curvature to minimize the Helfrich's bending energy as can be seen in Fig. 10. In this figure the square symbol represents the same material point on the membrane during the tank-treading motion. As the material point rotates around the internal fluid, the capsule is elongated and compressed by the shear flow periodically.

If we increase the bending modulus further the motion of the capsule will change from swinging to tumbling as observed for the oblate spheroid. In tumbling motion, raising bending modulus also restricts the deformation of the capsule from the initial shape. Figure 11 shows the results for another set of simulations with $\lambda=4$ and $G=0.1$. Unlike in swinging mode, raising bending modulus in tumbling mode reduces the oscillation in the deformation parameter. In terms of the inclination angle, raising bending modulus reduces the rotation periods as seen in Fig. 11(b). Figure 12 shows snapshots of a biconcave capsule during tumbling motion. Again, when there is bending stiffness the capsules try to keep the instantaneous curvature as closed as possible to the initial curvature to minimize the Helfrich's bending energy. Without bending modulus, as the capsule rotates the dimple becomes deeper and sharper at certain points in time as observed in [29]. The surface area of the biconcave capsules in our simulations varies by 0.5–1.0 %, which is consistent to the fact that red blood cells deform at near constant area.

IV. CONCLUSIONS

We have studied the effect of bending stiffness on the deformation and motion of liquid capsules enclosed by thin shell in shear flow using the implicit immersed boundary method. We have developed a formulation for describing

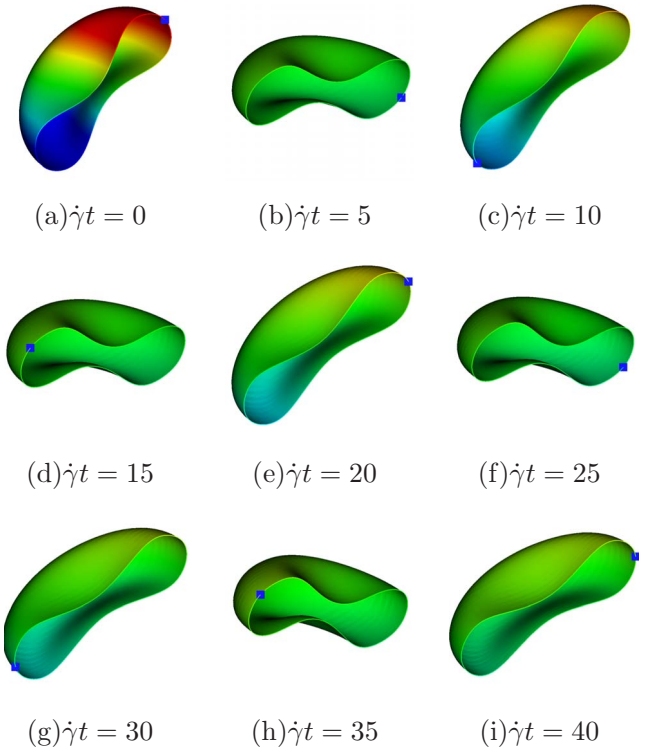

FIG. 12. (Color online) Shapes of the biconcave capsules at $G=0.1$, $\lambda=4$, and $\hat{\kappa}_B=0.04$ during a tumbling motion. The colors represent the x component of the velocity on the surface of the capsule.

elastic tensions and bending moments developing on the thin-shell middle surface during the capsule deformation. The strict requirement of surface area incompressibility on membranes consisting of lipid bilayers has not been included in the present formulation. However, by using very large area dilatation in the strain-energy function, the total surface area of the red blood cell membrane varies within 1% during both tank-treading and tumbling motions. Numerical results for capsules with spherical, oblate spheroidal, and biconcave unstressed shapes have confirmed that the bending stiffness restricts the overall deformation of capsules. And raising the bending stiffness can lead to the transition of motion modes of oblate spheroid and biconcave capsules from tank treading to tumbling. In addition, raising the bending stiffness increases the oscillation in the deformation parameter in tank-treading mode but reduces the oscillation in tumbling mode.

[1] N. Mohandas and E. Evans, Annu. Rev. Biophys. Biomol. Struct. **23**, 787 (1994).
[2] K. Chang and W. Olbricht, J. Fluid Mech. **250**, 609 (1993).
[3] A. Walter, H. Rehage, and H. Leonhard, Colloid Polym. Sci. **278**, 169 (2000).
[4] A. Walter, H. Rehage, and H. Leonhard, Colloids Surf., A **183-185**, 123 (2001).
[5] T. M. Fischer, Biophys. J. **86**, 3304 (2004).
[6] M. Abkarian, M. Faivre, and A. Viallat, Phys. Rev. Lett. **98**, 188302 (2007).
[7] D. Barthès-Biesel, J. Fluid Mech. **100**, 831 (1980).
[8] D. Barthès-Biesel and J. M. Rallison, J. Fluid Mech. **113**, 251 (1981).
[9] J. M. Skotheim and T. W. Secomb, Phys. Rev. Lett. **98**, 078301 (2007).
[10] H. Noguchi, Phys. Rev. E **80**, 021902 (2009).
[11] C. Eggleton and A. Popel, Phys. Fluids **10**, 1834 (1998).
[12] S. Ramanujan and C. Pozrikidis, J. Fluid Mech. **361**, 117

(1998).
[13] C. Pozrikidis, J. Fluid Mech. **440**, 269 (2001).
[14] E. Lac, D. Barthès-Biesel, N. Pelekasis, and J. Tsamopoulos, J. Fluid Mech. **516**, 303 (2004).
[15] Y. Sui, Y. T. Chew, P. Roy, X. B. Chen, and H. T. Low, Phys. Rev. E **75**, 066301 (2007).
[16] S. K. Doddi and P. Bagchi, Phys. Rev. E **79**, 046318 (2009).
[17] P. Bagchi and R. M. Kalluri, Phys. Rev. E **80**, 016307 (2009).
[18] S. Keller and R. Skalak, J. Fluid Mech. **120**, 27 (1982).
[19] J. Deschamps, V. Kantsler, and V. Steinberg, Phys. Rev. Lett. **102**, 118105 (2009).
[20] C. Misbah, Phys. Rev. Lett. **96**, 028104 (2006).
[21] M. Abkarian and A. Viallat, Soft Matter **4**, 653 (2008).
[22] Y. Sui, H. T. Low, Y. T. Chew, and P. Roy, Phys. Rev. E **77**, 016310 (2008).
[23] S. Kessler, R. Finken, and U. Seifert, J. Fluid Mech. **605**, 207 (2008).
[24] D. Le and Z. Tan, J. Comput. Phys. **229**, 4097 (2010).
[25] R. Lipowsky, Nature (London) **349**, 475 (1991).
[26] E. Cerda, S. Chaieb, F. Melo, and L. Mahadevan, Nature (London) **401**, 46 (1999).
[27] W. Helfrich, Z. Naturforsch. C **28**, 693 (1973).
[28] D. Le, J. White, J. Peraire, K. Lim, and B. Khoo, J. Comput. Phys. **228**, 8427 (2009).
[29] D. Le, Comput. Methods Appl. Mech. Eng. **199**, 2622 (2010).
[30] J. Stam, SIGGRAPH 1998 Proceedings, 1998 (unpublished).
[31] F. Cirak and M. Ortiz, Int. J. Numer. Methods Eng. **51**, 813 (2001).
[32] J. Simo and D. Fox, Comput. Methods Appl. Mech. Eng. **81**, 91 (1990).
[33] R. Skalak, A. Tozeren, R. Zarda, and S. Chien, Biophys. J. **13**, 245 (1973).
[34] C. Peskin, Acta Numerica **11**, 479 (2002).
[35] E. Evans and Y. Fung, Microvasc. Res. **4**, 335 (1972).
[36] X. Li and K. Sarkar, J. Comput. Phys. **227**, 4998 (2008).
[37] Y. Sui, Y. Chew, P. Roy, and H. Low, J. Comput. Phys. **227**, 6351 (2008).